Remote Sensing of Environment 201 (2017) 99–114

Contents lists available at ScienceDirect

Remote Sensing of Environment

journal homepage: www.elsevier.com/locate/rse

An evaluation of monthly impervious surface dynamics by fusing Landsat and MODIS time series in the Pearl River Delta, China, from 2000 to 2015

Lei Zhang[a,b,c], Qihao Weng[c,d,*], Zhenfeng Shao[b]

[a] School of Geodesy and Geomatics, Wuhan University, 129 Luoyu Road, Wuhan 430079, PR China
[b] State Key Laboratory of Information Engineering in Surveying, Mapping and Remote Sensing, Wuhan University, 129 Luoyu Road, Wuhan 430079, PR China
[c] Center for Urban and Environmental Change, Department of Earth and Environmental Systems, Indiana State University, Terre Haute, IN 47809, USA
[d] School of Geography, South China Normal University, Guangzhou 510631, PR China

ARTICLE INFO

Keywords:
Impervious surfaces
Time series
Landsat
MODIS
Pearl River Delta
Data/image fusion
Urban areas

ABSTRACT

Researchers have been attending increasingly to impervious surface dynamics to better understand the urbanization process and its impacts on urban environments. Previously, numerous studies have only estimated and mapped impervious surface dynamics at annual or decadal time scales. It is challenging to estimate impervious surface dynamics at a finer time scale, such as on a monthly scale, while using a single source of medium spatial resolution satellite imagery. However, urban infrastructure construction could cause changes in impervious surfaces in a short period of time. This paper aimed at developing a new methodology for evaluating monthly impervious surface dynamics by fusing Landsat and MODIS time series. The Pearl River Delta in China, is located in a humid subtropical region and was selected as the study area due to its dramatic urbanization in the past three decades. Available Landsat images with cloud cover < 90%, 7-Day MODIS NDVI 250 m smooth time series, and daily MODIS LST 1000 m time series from 2000 to 2015 were downloaded. These data were used to develop temporal features of land covers (i.e., monthly Landsat NDVI and LST time series) and to monitor impervious surface dynamics using semi-supervised time series fuzzy clustering method. The results showed the effectiveness of temporal features in differentiating land covers. Additionally, the average overall classification accuracy yielded reasonable accuracies (up to 89.36%). The proposed methodology has illustrated numerous, considerable advantages over previous methods. It has offered consistent maps of impervious surfaces on a monthly time scale as well as enhanced distinguishability of land covers with similar spectral characteristics. This study can be utilized to establish relationships between urban expansion, climate change, urban environment, population, and other socio-economic variables on a monthly basis. The study is also crucial for predicting the timing, duration, and density of ecological change for increased impervious surfaces.

1. Introduction

Impervious surfaces are a key variable for determining the degree of urbanization and environmental quality in cities. Numerous methods have been successfully employed for characterizing impervious surfaces at the local, regional, and continental scales, including spectral mixture analysis (Wu and Murray, 2003; Weng et al., 2008), regression (Yang et al., 2003; Yuan et al., 2008; Mohapatra and Wu, 2010), random forest (Zhang et al., 2014), and machine learning algorithms (Hu and Weng, 2009; Lu and Weng, 2009; Esch et al., 2009). Weng (2012) provided an overview of the methods for impervious surface estimation using remote sensing imagery at various spatial scales.

Researchers have been attending increasingly to impervious surface dynamics to better understand the urbanization process and its impacts on urban environments, rather than mapping impervious surfaces for a single date. For instance, Powell et al. (2008) quantified impervious surface change over 34 years (1972–2006) in the Snohomish Water Resource Inventory Area (WRIA), which illustrated the value of Landsat time series for monitoring impervious surface trends. Sexton et al. (2013) mapped annual dynamics of impervious surfaces from Landsat archive in Washington, D.C.–Baltimore, MD megalopolis from 1984 to 2010, which illustrated the potential of empirical retrieval of impervious coverage at spatial and temporal scales. Shao and Liu (2014) produced annual impervious surface fraction maps in the Yangtze River Delta, China, from 2000 to 2009, which demonstrated a method to monitor large-scale impervious surface dynamics.

However, previous methods focused mainly on impervious surface dynamics at annual or decadal time scales. Additionally, they were

* Corresponding author at: Center for Urban and Environmental Change, Department of Earth and Environmental Systems Indiana State University, Terre Haute, IN 47809, USA.
E-mail address: qweng@indstate.edu (Q. Weng).

http://dx.doi.org/10.1016/j.rse.2017.08.036
Received 30 December 2016; Received in revised form 18 August 2017; Accepted 25 August 2017
Available online 14 September 2017
0034-4257/

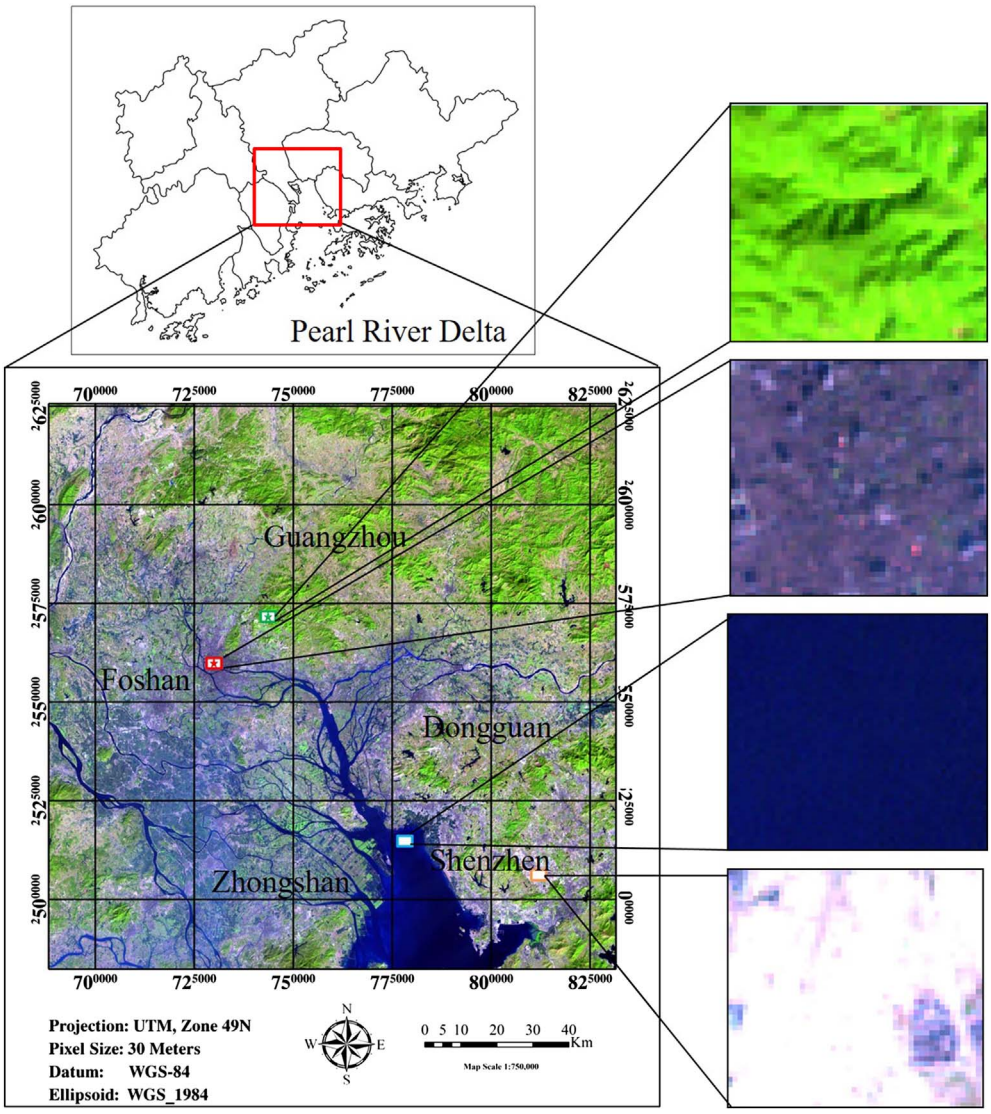

Fig. 1. Location and geographic extent of study area. The red rectangle stands for dark impervious surfaces; the orange rectangle bright impervious surfaces; the green rectangle pervious surface area; and the light blue rectangle water bodies. The red star is a representative impervious surface pixel; and the green star a representative pervious surface pixel. (For interpretation of the references to color in this figure legend, the reader is referred to the web version of this article.)

more concerned on increasing mapping accuracy of impervious surfaces for each date. Although these methods used multi-temporal or time series imagery, they mainly utilized spectral characteristics of land covers from single date image to differentiate land covers. Other methodologies utilized both spectral and spatial characteristics of land covers to map impervious surface dynamics by integrating medium and high resolution imagery. Lu et al. (2011) integrated multi-temporal Landsat and QuickBird images to monitor impervious surface change in Lucas do Rio Verde County, Brazil, which showed the effectiveness in fixing mixed pixel problems in urban–rural frontiers. Gao et al. (2012) developed a time series of consistent impervious surface maps using medium-resolution satellite images in the Yangtze River Delta, China. Nevertheless, these methods did not address the temporal characteristics of land covers from multi-temporal or time series imagery. Temporal profiles provide useful information that can enhance the identification of vegetation phenology as well as the trends and timing of changes (Ratana et al., 2005; Lunetta et al., 2006; Ma et al., 2013). Therefore, this study intended to explore the usage of temporal characteristics of land covers for mapping impervious surface dynamics at a monthly time scale.

The key for extracting the temporal characteristics of land covers is to utilize the temporal resolution of satellite imagery. Lunetta et al. (2004) suggested that an increment in temporal data acquisition frequencies helped to reduce omission errors of changes; change events largely determined the nominal temporal frequency of remote sensing data acquisitions. Changes in impervious surfaces have no fixed dates, because the changes mainly result from urban expansion, social-economic development and planning. As a result, the impervious surfaces may change inter-yearly, seasonal, monthly, or more frequently. Thus, it is necessary to map impervious surface dynamics on a finer time scale. Additionally, high temporal resolution is helpful for discerning the spatiotemporal patterns of change and differentiating the temporal characteristics of land covers. Recently, some image fusion models have been proposed to increase temporal resolution of medium spatial resolution satellite data, such as STARFM (Gao et al., 2006), STAARCH (Hilker et al., 2009), ESTARFM (Zhu et al., 2010), SADFAT (Weng et al. 2014), and FSDAF (Zhu et al., 2016). This study applied FSDAF to fuse Landsat and MODIS data for improving temporal resolution of the time series.

This study aimed at developing a new methodology to map impervious surfaces on a monthly basis using Landsat time series. Available Landsat data are often irregularly acquired due to cloud contamination, weather conditions and sensor failure. This is especially true for tropical or subtropical humid regions, such as the Pearl River Delta (PRD), China. The PRD region, with a subtropical climate, annual mean temperature of 21–23 °C and annual precipitation of 1500–2500 mm, has a wet season from April to October. Thus, there is a great chance for obtaining numerous cloud-contaminated Landsat

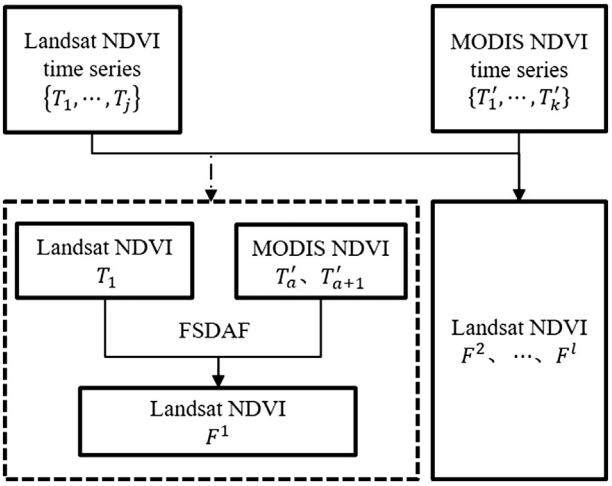

Fig. 2. Procedure for fusion of Landsat NDVI and MODIS NDVI images.

images. Key issues for monitoring impervious surface dynamics on a fine time scale in PRD are improving the temporal resolution of usable Landsat data and identifying different temporal characteristics of land covers in time series. To address these issues, this study presented an efficient method to produce monthly impervious surface maps from data based on temporal spectral features that was collected from 2000 to 2015. Due to the positive relationship between LST (Land Surface Temperature) and impervious surfaces and the apparent inverse relationship between NDVI (Normalized Difference Vegetation Index) and impervious surfaces (Yuan and Bauer, 2007; Zhang et al., 2009; Li et al., 2011), this study derived temporal features from monthly Landsat NDVI and LST time series.

2. Study area and datasets

The Pearl River Delta, which is located in southern China, covers 56,000 km^2 in area and had a population of 56 million in 2012. It has been named as the largest urban agglomeration in the world both in size and population by the World Bank Group. Fig. 1 shows the study area with a false color composite image using Landsat OLI (October 18, 2015) bands 6, 5, and 4. The PRD has experienced rapid urbanization since China's reform and opening up in 1978, and this trend has continued through the 21st century. A total of 419 Landsat images with cloud cover < 90%, spanning from 2000 to 2015, were downloaded from USGS EarthExplorer (Reference system: WRS-2, Path: 122, Row: 44). The study area, covering an area of 20,542 km^2, was a subset of the downloaded Landsat imagery. The 7-Day MODIS NDVI 250 m smooth time series were ordered and downloaded from a freely web application for executing pre-processing operations of standard MODIS Vegetation-Index (VI) products (http://ivfl-info.boku.ac.at/). The web application was developed by the University of Natural Resources and Applied Life Sciences (BOKU) in Vienna, Austria, which provides on-demand smoothed and/or raw satellite time series of MODIS Vegetation Indices (VI). The preprocessing methods include reprojection, image mosaicking, smoothing and gap filling (Vuolo et al., 2012). Daily MODIS LST 1000 m time series were derived from Aqua MODIS MYD11_L2 (version 5) products from the LAADS web (http://ladsweb.nascom.nasa.gov) (Aqua Land Level 2 products).

3. Methods

3.1. Data preprocessing

There was missing information in the Landsat image data due to cloud contamination, weather conditions, and sensor failure. Since missing data is a major source of uncertainty in satellite observations (Wang et al., 2012; Kondrashov and Ghil, 2006), it is crucial that this problem is solved. Below are the procedures used in this study:

Clouds, cloud shadows, and snows were isolated by using the Fmask algorithm (Zhu and Woodcock, 2012) for all Landsat scenes. Further, the Modified Neighborhood Similar Pixel Interpolator (NSPI) (Zhu et al., 2012a) was applied to remove thick clouds in Landsat subsets. A cloud-free Landsat image acquired in the same year was selected as the auxiliary image for cloud removal in the Landsat subsets. Next, the Geostatistical Neighborhood Similar Pixel Interpolator (GNSPI) (Zhu et al., 2012b) was applied to fill gaps in Landsat ETM + SLC-off images. Since the combination of NDVI and LST has proved to be valuable in differentiating land covers (Son et al., 2012; Han et al., 2010; Julien et al., 2011), Landsat NDVI and LST time series were derived from the gap-filled Landsat data for later use. LST was calculated by using the radiative transfer equation with corrections of atmospheric effect and land surface emissivity (Zhang and Weng, 2016).

3.2. Fusion of Landsat and MODIS data

Potential error from the gap filling may have caused uncertainty in the development of temporal spectral features. To minimize the chance for error, this study employed Flexible Spatiotemporal Data Fusion (FSDAF) (Zhu et al., 2016) to produce dense Landsat NDVI/LST time series by fusing available Landsat NDVI/LST time series and MODIS NDVI/LST time series. FSDAF integrated spectral unmixing analysis, spatial interpolation and STARFM into a single framework. Additionally, FSDAF has shown advantages over some existing spatio-temporal data fusion methods (Zhu et al., 2016). For each month, Landsat images with cloud cover over 50% were predicted based on FSDAF using time-adjacent MODIS images. If all Landsat images in a month possessed cloud cover over 50%, all images in this month were considered unavailable. Fig. 2 shows the procedure for fusion of Landsat NDVI and MODIS NDVI in the ith month.

Given available Landsat NDVI time series in year $Y = \{L_1, L_2, \cdots, L_{12}\}$, $L_i (1 \le i \le 12)$ represented Landsat NDVI image set $\{L_i^1, \cdots, L_i^j\}$ in the ith month, where j was number of images in the ith month, and $\{T_1, \cdots, T_j\}$ was its correspondent image sequence in the ith month. For 7-Day MODIS NDVI time series in the same year $Y = \{M_1, M_2, \cdots, M_{12}\}$, $M_i (1 \le i \le 12)$ represented MODIS NDVI image set $\{M_i^1, \cdots, M_i^k\}$ in the ith month, where k was the number of images in the ith month, and $\{T_1', \cdots, T_k'\}$ was its correspondent image sequence in the ith month.

In the ith month, image L_i^1 at date T_1 was selected as the base image for prediction of Landsat NDVI image F_i^1 using MODIS NDVI image $M_i^a (1 \le a \le k)$ at date T_a' (T_a' is the closest date to T_1) and MODIS NDVI image M_i^{a+1} at date T_{a+1}'. Then, image L_i^2 at date T_2 was used as the base image to predict F_i^2. Thus, in the ith month of year Y, Landsat NDVI $\{F_i^1, \cdots, F_i^l\}$ images in the ith month were predicted.

If there was no available Landsat image in the ith month, Landsat NDVI image with least cloud cover in the $(i-1)$th month L_{i-1} at date T_{i-1} would be selected as the base image for predicting Landsat NDVI images in the ith month. Landsat NDVI image F_i^1 was predicted by using MODIS NDVI image M_{i-1} at adjacent date T_{i-1}' and MODIS NDVI image M_i^1 at date T_1'. Thus, in the ith month of year Y, Landsat NDVI $\{F_i^1, \cdots, F_i^l\}$ images in the ith month were predicted.

Fig. 3 shows the procedure for fusion of Landsat LST and MODIS LST in the ith month. Given available Landsat LST time series in year $Y = \{S_1, S_2, \cdots, S_{12}\}$, $S_i (1 \le i \le 12)$ represented Landsat LST image set $\{S_i^1, \cdots, S_i^j\}$ in the i^{th} month, where j was the number of images in the ith month, and $\{\overline{T}_1, \cdots, \overline{T}_j\}$ was its corresponding image sequence in the ith month. For daily MODIS LST time series in the same year $Y = \{MS_1, MS_2, \cdots, MS_{12}\}$, $MS_i (1 \le i \le 12)$ represented MODIS LST image set $\{MS_i^1, \cdots, MS_i^k\}$ in the ith month, where k was the number of images in the ith month, and $\{\overline{T}_1', \cdots, \overline{T}_k'\}$ was its corresponding image sequence in the ith month. For Landsat LST image S_i^1 and its date $\overline{T}_1$, one MODIS LST image MS_i^1 with the same time date $\overline{T}_1$ and one time-adjacent image

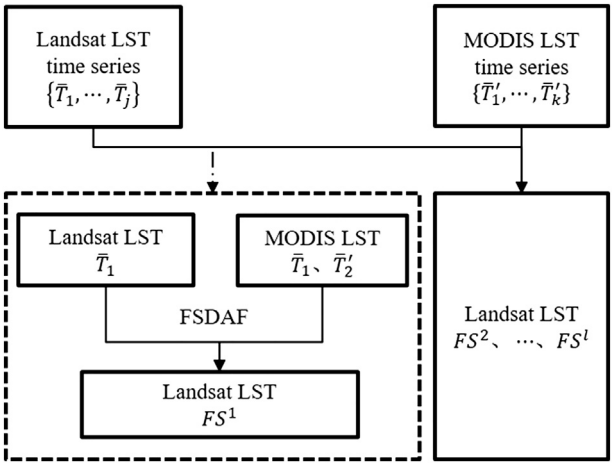

Fig. 3. Procedure for fusion of Landsat LST and MODIS LST images.

MS_i^2 at date $\bar{T}'_2$ were used to predict Landsat LST image FS_i^1 at date $\bar{T}'_2$. If there was no available Landsat images in the ith month, Landsat LST image with least cloud cover in the $(i-1)$th month L_{i-1} at date T_{i-1} would be selected as the base image for predicting Landsat LST images in the ith month. Thus, in the ith month of year Y, Landsat LST $\{FS_i^1, \cdots, FS_i^l\}$ images in the ith month were predicted.

3.3. Generation of monthly Landsat NDVI and LST time series

Dense Landsat NDVI and LST time series were developed by fusing Landsat and MODIS data. However, since the dense Landsat NDVI/LST time series were unevenly distributed, it was difficult to extract obvious and regular temporal parameters, such as trend values averaged over certain time intervals. To address this issue, monthly Landsat NDVI/LST time series were generated in this study. Fig. 4 shows the process for producing monthly Landsat NDVI/LST time series in each year.

Locally weighted linear regression was conducted as a non-parametric algorithm to develop a composited image in the ith month of year Y by using MATLAB (MATLAB R2013a, The MathWorks Inc. Natick, MA). Landsat NDVI time series $\{L_i^1, \cdots, L_i^j, F_i^1, \cdots, F_i^l\}$ in the ith month of year Y, where l was the number of predicted Landsat NDVI images, were made as a single NDVI image composite in the ith month. Firstly, Landsat NDVI time series $\{L_i^1, \cdots, L_i^j, F_i^1, \cdots, F_i^l\}$ was rearranged by cloud cover percentage as Landsat NDVI time series $\{L_i^1, \cdots, L_i^m\}$, where m was the number of total images in that month and $m = j + l$. Considering the problem of predicting reflectance value r of pixel p with coordinate (x,y) in the composited image, following objective function needed to be minimized:

$$r(\theta) = \sum_m w^m (p^m - \theta^T p)^2 \quad (1)$$

where p^m represented cloud cover percentage of pixels with same coordinate in Landsat NDVI time series $\{L_i^1, \cdots, L_i^m\}$. w^m were weights for pixels with coordinate (x,y) in new image sequence.

$$w^m = exp\left(-\frac{(p^m - p)^2}{2\tau^2}\right) \quad (2)$$

If $|p^m - p|$ was small, w^m was close to 1. If $|p^m - p|$ was large, w^m was small. τ was the parameter to control how quickly the weight values fell off with cloud cover differences. Similarly, any Landsat LST time series $\{L_i^1, \cdots, L_i^j, FS_i^1, \cdots, FS_i^l\}$ in the ith month of year Y was also composited into one LST image using the locally weighted linear regression.

3.4. Time series decomposition

Most data mining methods cannot be used effectively on time series data without a dimension reduction (Keogh et al., 2001). Time series decomposition enables distinctions among various types of change, such as disturbances and phenological changes. In this study, time series decomposition was used as a dimension reduction method to map each time series to a lower-dimensional space for extracting temporal features. The details of the procedure are explained below.

Monthly Landsat NDVI and LST images from 2000 to 2015 were obtained as NDVI time series $\{NI_1, NI_2, \cdots, NI_q\}$ and LST time series $\{LT_1, LT_2, \cdots, LT_q\}$, where $q = 192$ was the number of months during the study period. Then, monthly NDVI/LST time series were decomposed into three additive components:1) trend component; 2) seasonal component; and 3) irregular component. The trend component defined gradual change that was caused by land expansion and degradation; the seasonal component depicted seasonal change that was caused by vegetation phenology; and the irregular component characterized abrupt change caused by disturbances. An additive decomposition model was applied to separate monthly NDVI/LST time series into these three distinct components.

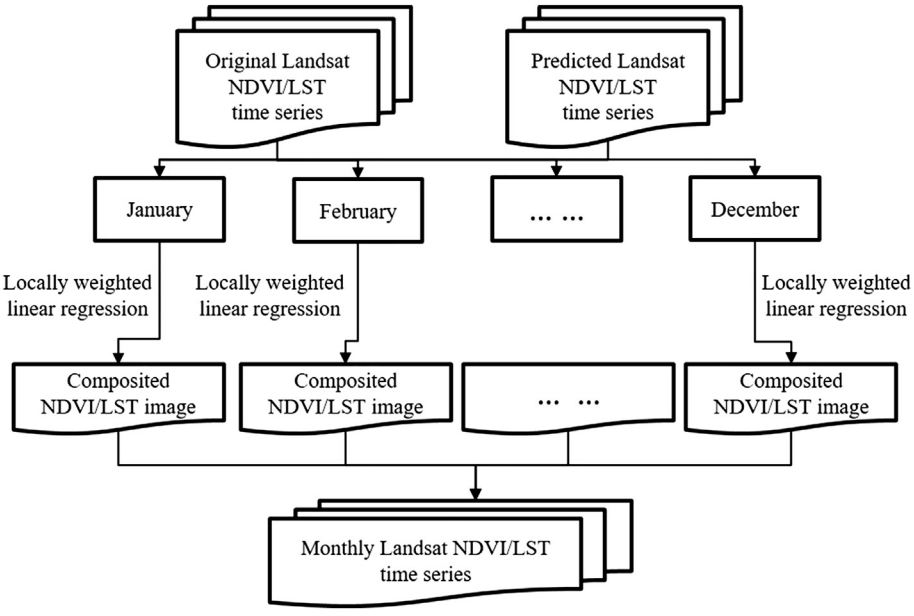

Fig. 4. Generation of monthly Landsat NDVI/LST time series.

$$X_t = T_t + S_t + I_t \quad (3)$$

where $t = 1, \cdots, q$, X_t was variable value at time t, T_t was trend component, S_t was seasonal component, and I_t was irregular component. T_t was estimated using parametric regression model.

$$T_t = \alpha_0 + \alpha_1 t + \alpha_2 t^2 \quad (4)$$

Since de-seasonalized time series was helpful for comparison among time series with different seasonal patterns (Cleveland and Tiao, 1976), seasonal adjustment was performed as an iterative process to estimate the optimal trend component. Thus, the seasonal component was estimated by applying a stable seasonal filter to de-trended time series.

Due to the seasonal component having a periodicity of 12 in the monthly time series, a 13-term moving average was used to smooth the data. Additionally, the first and last smoothed values were repeated six times to prevent observation loss. Next, the original time series would be subtracted by the smoothed time series to obtain the first detrended time series $DT_t = X_t - T_t$. Meanwhile, seasonal indices were created as $In_{n \times m}$, where n is number of year and $m = 12$. In_i was a m dimensional vector with elements i, $i + 12$, $i + 12 \times 2$, $\cdots$, $i + 12 \times (n - 1)$ and $i = (1, 2, \cdots, n)$. That is, In_1 means all indices values of January from 2000 to 2015, and In_i means all indices values of the ith month from 2000 to 2015. All of indices values In_i for each month in the detrended time series DT_t would be averaged to center seasonal estimate to fluctuate around zero. Thus, S_t had a constant amplitude across the time series.

After that, deseasonalized time series $DS_t = X_t - S_t$ was obtained. Further, the second estimation of trend component $\widehat{T_t}$ was obtained using deseasonalized time series DS_t. Next, the second detrended time series could be obtained as $\widehat{DT_t} = X_t - \widehat{T_t}$. Then, the second estimation of seasonal component $\widehat{S_t}$ was estimated by applying a seasonal filter to $\widehat{DT_t}$. Finally, deseasonalized time series $\widehat{DS_t} = X_t - \widehat{S_t}$ was calculated after deseasonalizing original time series. Since deseasonalized time series consisted of long-term trend and irregular components, irregular component was estimated as $\widehat{I_t} = \widehat{DS_t} - \widehat{T_t}$. Then, trend measure $1 - \frac{var(\widehat{I_t})}{var(\widehat{DS_t})}$ and seasonality measure $1 - \frac{var(\widehat{I_t})}{var(\widehat{DT_t})}$ were calculated. Additionally, sum, mean, median, minimum, and maximum values of seasonal component $\widehat{S_t}$ were calculated at each season point over the seasonal cycle, which was set as four. These statistics, which considered as temporal features, were next used for fuzzy clustering.

3.5. Time series fuzzy clustering

Time series clustering categorizes time series by minimizing dissimilarity of patterns in same cluster while maximizing dissimilarity of different clusters (Liao, 2005; Fu, 2011). Since Fuzzy C-means (FCM) (Bezdek et al., 1984) has been shown to be effective in time series analysis (Futschik and Kasabov, 2002; Li et al., 2008; Egrioglu et al., 2013), this study developed a semi-supervised FCM clustering algorithm to cluster temporal features. Dynamic time warping (DTW) distance was introduced in the proposed method to find optimal cluster centers. DTW was selected over Euclidean distance because DTW has been shown to be effective in finding an optimal match between two distinct time series and in evaluating similarity based on the shapes of the time series (Jeong et al., 2011).

Given a representation of temporal features, this study aimed at finding c classes based on measures of dynamic time warping distance. For time series $X = \{x_1, x_2, \cdots, x_{n'}\}$, $x_k \in R^d (k = 1, 2, \cdots, n')$, d was the dimension of temporal features derived from time series decomposition, n' was the number of samples. FCM clustered X into c fuzzy subsets by minimizing the following objective function:

$$O(U, V) = \sum_{k=1}^{c} \sum_{j=1}^{n'} u_{kj}^m d_{jk}^2 \quad (5)$$

$$d_{jk}^2 = d(x_j, v_k)^2 \quad (6)$$

where c was the number of clusters, u_{kj} was membership of x_j in class k, m was clustering fuzziness coefficient. The membership matrix U was constrained to contain elements in the range [0,1] and $\Sigma_{k=1}{}^{c} u_{kj} = 1, \forall j = 1, 2, \cdots, n'$. The matrix $V = \{v_1, v_2, \cdots, v_c\}$ was set of cluster centers. $d()$ was dynamic time warping distance between pixel x and cluster center v. The objective function O was minimized by alternate iterative algorithm. Then, the partition matrix was calculated as follows:

$$u_{kj} = \frac{1}{\sum_{q=1}^{c} \left(\frac{d(v_k, x_j)}{d(v_q, x_j)} \right)^{2/(m-1)}} \quad (7)$$

The pseudo code for calculating DTW distance between two time series can be found in Petitjean et al. (2011). However, it was difficult to use DTW distance to calculate average of a set of time series. The averaging method in Petitjean et al. (2011) was applied to calculate cluster centers in order to calculate the average of the time series based on DTW distance.

Since FCM was sensitive to initialization, this study proposed a semi-supervised FCM to incorporate prior information about clusters into the FCM algorithm to improve clustering performance. This semi-supervised method can effectively address the problem of clustering with limited labeled data and large amount of unlabeled data. Given time series X consisting of X_l and X_u, X_l represented labeled time series samples and X_u represented unlabeled time series samples, the whole process of semi-supervised FCM algorithm was shown as: (1) Initialized values of m and u_{kj} using X_l and X_u. For X_l, value of component u_{kj} was set to 1 if data x_j was labeled with class k, and 0 otherwise. For X_u, positive random values within [0,1] were set to unlabeled data. The initial set of centroid v_k was calculated as $v_k^0 = \frac{\sum_{j=1}^{n'} (u_{kj}^l)^m x_j^l}{\sum_{j=1}^{n'} (u_{kj}^l)^m}$, where n′ was number of labeled data. (2) Updated membership u_{kj} in X_u and centroid v_k until the objective function was minimized.

3.6. Two-scale temporal filtering

Temporal filtering has been applied successfully to improve the consistency of time series classification (Zhang and Weng, 2016). Based on the assumption that the urbanization was an irreversible process, this study developed a two-scale temporal filtering method to check the sequences of land cover changes and to correct classification errors. The procedure of two-scale temporal filtering was as follows:

Step 1: Building a large-scale temporal window on a yearly basis. Given annual clustering maps $Y = \{y_1, y_2, \cdots, y_n\}$, n was the number of years. y_i was the map with highest classification accuracy in the ith year, $i = 1, 2, \cdots, n$. The size of each temporal window was set as 3 × 3. Since the effectiveness of temporal filtering largely depended on the initial image, we selected the image with highest classification accuracy in Y as the initial image y_k.

Step 2: Comparing land covers in the temporal window $\{y_{k-1}, y_k, y_{k+1}\}$. If the pixel p had the same geographic location in image y_{k-1} and image y_{k+1} were labeled as pervious surface, but in image y_k, pixel p was labeled as impervious surface, then, the pixel p in image y_k was identified as uncertain pixel.

Step 3: Determining the class of pixel p in image y_k. If p in image y_{k+2} was pervious surface, p in image y_k was corrected as pervious surface. If p in image y_{k+2} was impervious surface, then, p in image y_{k+1} was identified as uncertain pixel.

Step 4: Applying the moving temporal window to the yearly time series, beginning in y_{k-1} and y_{k+1} bidirectionally, and proceeding to y_{k-2} and y_{k+2}. After the large-scale temporal filtering, the original annual clustering maps $Y = \{y_1, y_2, \cdots, y_n\}$ were corrected as $Y' = \{y_1', y_2', \cdots, y_n'\}$.

Step 5: Applying a small-scale temporal window on a monthly basis. The size of temporal window was set as 3 × 3. The small-scale temporal window was used to correct classification errors in each month within a year. In the kth year, the beginning image was y_k', because y_k' has the highest classification accuracy in that year. Similar to the large-scale

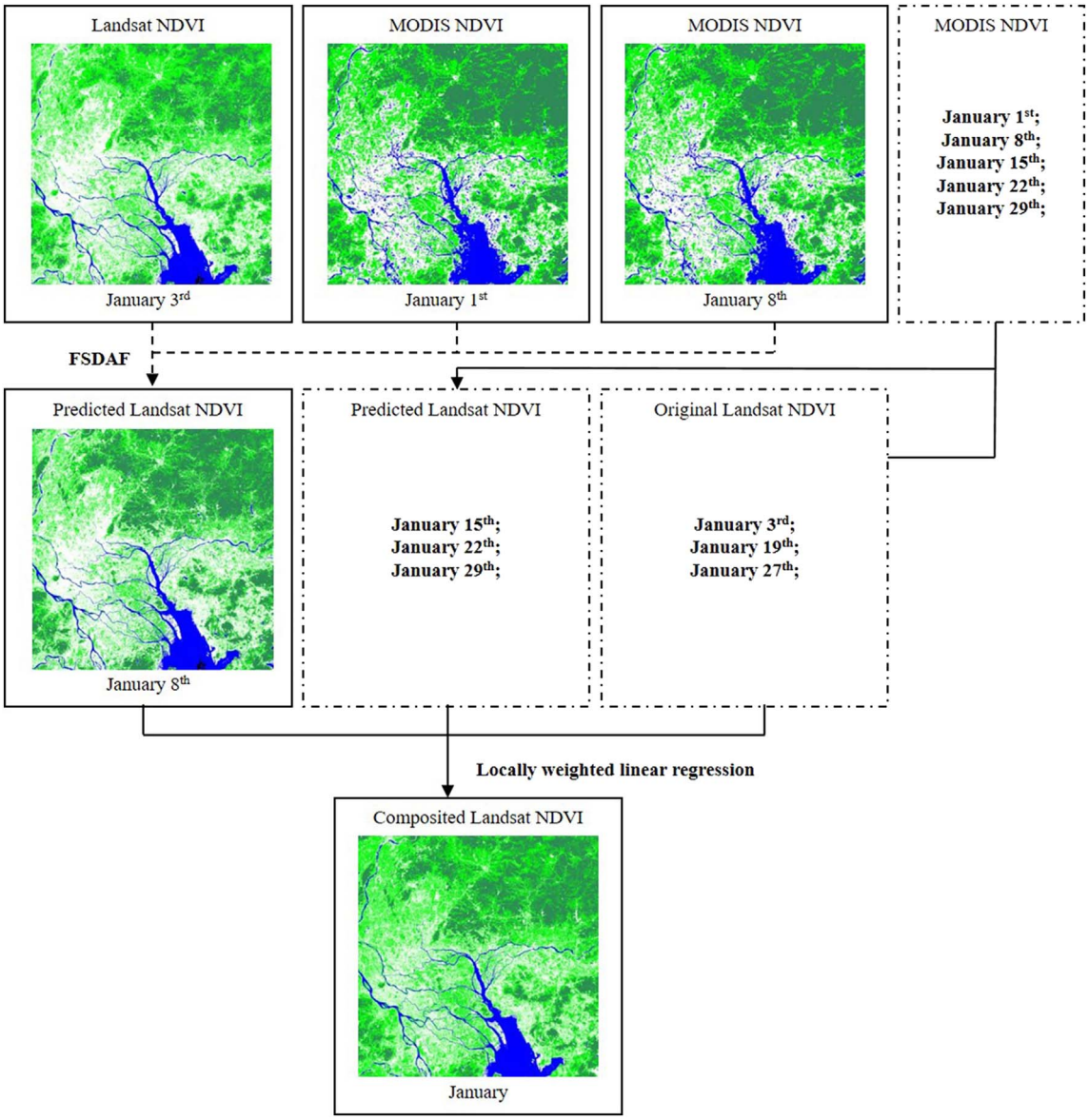

Fig. 5. Example of a generated composite Landsat NDVI image in January 2015. (For interpretation of the references to color in this figure, the reader is referred to the web version of this article.)

temporal window, the small-scale moving window was applied to the monthly time series, beginning in y_k' bidirectionally, and proceeding to y_{k-1}' and y_{k-1}' monthly.

4. Results

4.1. Monthly Landsat NDVI/LST images

Figs. 5 and 6 show examples of generated NDVI/LST composite images in January 2015. In Fig. 5, green color represents pervious surfaces, blue color represents water bodies, and white color represents impervious surfaces. In Fig. 6, red color represents land cover with high land surface temperature, and blue color represents land cover with low temperature.

For producing monthly Landsat NDVI/LST images, FSDAF was applied to fuse Landsat and MODIS data to improve temporal resolution of the time series as well as to reduce uncertainty from gap filling. In order to obtain consistent Landsat NDVI/LST images in January 2015, Landsat NDVI/LST images were predicted for January 8th, January 15th, January 22th, and January 29th according to available dates of Landsat NDVI/LST images and MODIS NDVI/LST images in January. Then, predicted Landsat NDVI/LST images and original Landsat NDVI/LST images in January were combined into a single composite NDVI/LST image using locally weighted linear regression. The composited NDVI/LST dataset not only improved spatial details of available Landsat NDVI/LST images with cloud contamination, but also maintained good images of spectral characteristics.

4.2. Time series separability of land covers

This study differentiated impervious surfaces and other land covers based on differences in temporal characteristics of land covers. Fig. 7 shows temporal characteristics of land covers derived from original NDVI time series. Fig. 8 shows temporal characteristics of land covers derived from the composited monthly NDVI time series. Fig. 9 shows temporal characteristics of land covers derived from original LST time series. Fig. 10 shows temporal characteristics of land covers derived from the composited monthly LST time series. In order to minimize the effect of missing data caused by atmospheric and sensors problem, land cover samples that experienced no change over time were selected for

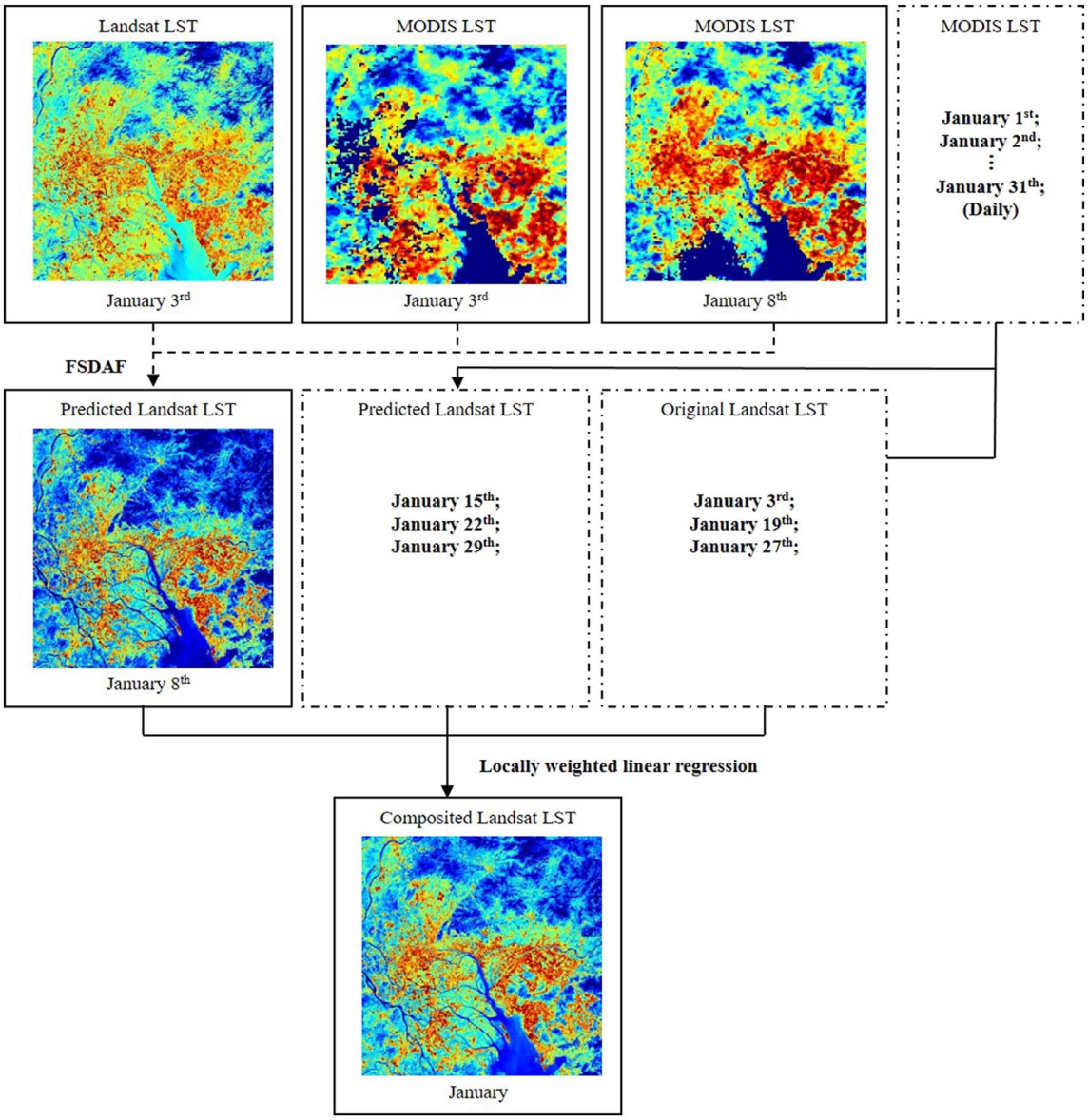

Fig. 6. Example of a generated composite Landsat LST image in January 2015. (For interpretation of the references to color in this figure, the reader is referred to the web version of this article.)

mapping temporal characteristics. This study assumed that urban growth was an irreversible change process and impervious surfaces represented an irreversible land cover. Thus, impervious surface samples were manually selected in the early images, and pervious surface samples and water bodies were manually selected in the most recent images. Selected impervious surface areas, pervious surface areas and water bodies are shown in white rectangles in Fig. 1.

As shown in NDVI time series in Figs. 7 and 8, pervious surfaces such as grass, forest, and agriculture had the highest surface reflectance values, while water bodies had the lowest surface reflectance values,

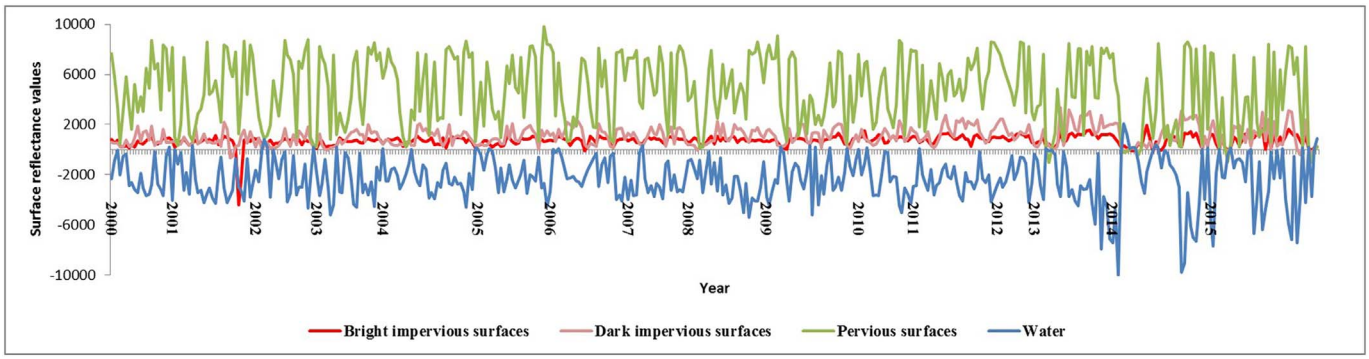

Fig. 7. Temporal characteristics of land covers derived from original NDVI time series.

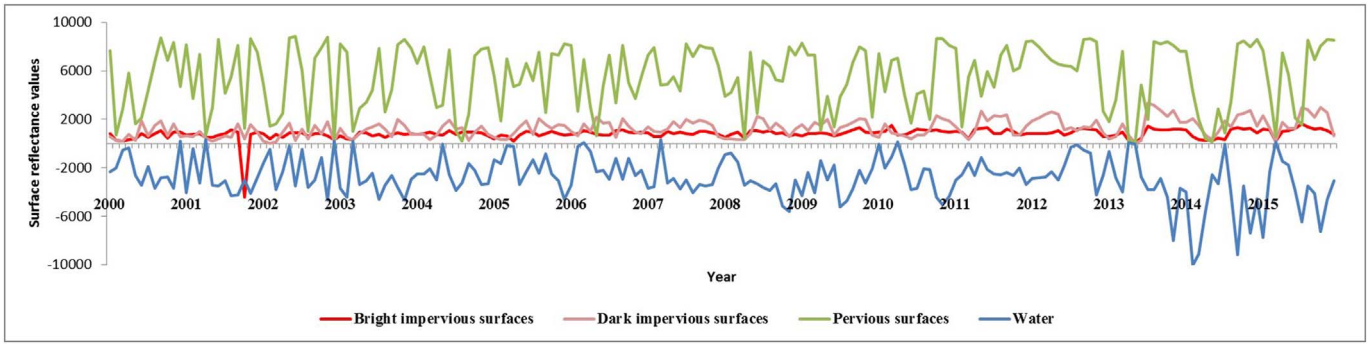

Fig. 8. Temporal characteristics of land covers derived from composited monthly NDVI time series.

and dark impervious surfaces had relatively higher surface reflectance values than bright impervious surfaces. However, in the two figures, both temporal characteristics of impervious surfaces in 2001 had abnormally low surface reflectance values. This was due to all impervious surface samples being SLC-off data in the Landsat NDVI image on Oct 27th, 2001. These abnormal points would be identified and processed using the following time series decomposition method. As shown in LST time series in Figs. 9 and 10, impervious surfaces had relatively higher temperatures, pervious surfaces had lower temperatures, and water bodies had the lowest temperatures.

In order to extract phenological characteristics of land covers from time series data, time series decomposition was conducted for each pixel. Fig. 11 shows time series components of a pervious surface pixel in monthly NDVI time series, where SR values represented surface reflectance values. The pervious surface pixel was shown in Fig. 1 as the green star. Fig. 12 shows time series components of an impervious surface pixel in monthly LST time series. The impervious surface pixel was shown in Fig. 1 as the red star.

As shown in Figs. 11 and 12, time series decomposition was helpful for detecting land cover change within the trend component that were influenced by disturbances, within the seasonal component that were heavily influenced by seasonal variations, and within the irregular component that were influenced by noise. Finally, temporal features were derived from the statistics of these time series components. In order to check whether temporal features could improve time series separability of land covers, DTW distance was applied in order to calculate within-class distances and between-class distances of land covers. Table 1 shows DTW distances of land covers derived from original time series, monthly time series and temporal features.

The DTW distance adapted accordingly to changed time nodes and tolerated the offset of spectral values on the time axis. Moreover, it was illustrated the DTW distance is capable of calculating the distances of temporal profiles at different time scales. Thus, the DTW distance was used for assessing the separability of land covers. The DTW distance ranged from 0 to 1, and land cover separability increased when the value approached 1. One hundred samples per class were randomly selected to calculate the mean value of DTW distance between land covers. Generally, between-class distances of land covers were higher than 0.5 and within-class distances were lower than 0.5. Table 1 shows that the monthly time series data outperformed the original time series data as the separability between bright impervious surfaces and pervious surfaces was improved, and as well as the separability between impervious surfaces and water. Additionally, the monthly time series data allowed for a decrease for the within-class distances of pervious surfaces and within-class distances of water and the data allowed for an increase for the within-class distances of different types of impervious surfaces. Therefore, the monthly time series data illustrated that it worked effectively on pervious surfaces, but needs improvement on impervious surfaces. Table 1 further showed that the monthly time series data was more effective in extracting phenological information than the original time series data. For temporal spectral features, the within-class distances of bright impervious surfaces, dark impervious surfaces, and water largely decreased, whereas the between-class distances between all types of impervious surfaces and pervious surfaces increased. Additionally, the within-class distance of pervious surfaces increased. This may be attributed to the selection of samples in different phenological phase. In conclusion, temporal spectral features illustrated effectiveness in improving time series separability of land covers, which essentially decreased within-class distances and increased most between-class distances of land covers.

4.3. Analysis of impervious surface dynamics

In contrast to conventional methods of estimating impervious surfacs at annual or multi-decadal time scales, this study aimed at monitoring impervious surface dynamics on a monthly frequency. This study also used the semi-supervised time series fuzzy clustering method to meet the application requirements of regional sustainable development. In fact, urban infrastructure construction could cause changes in impervious surfaces in a short period of time, which is especially true in rapidly urbanizing areas such as the PRD region, China. Monthly maps of impervious surfaces can swiftly identify the location, rate, and

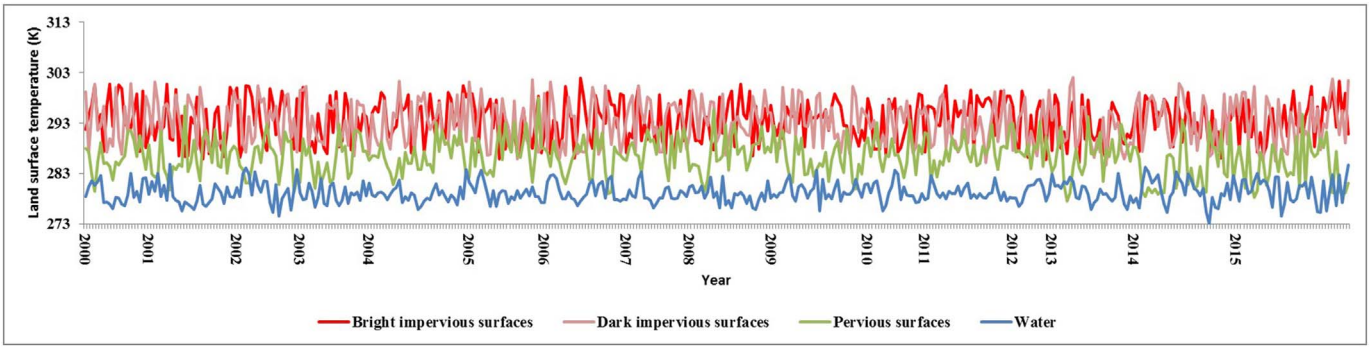

Fig. 9. Temporal characteristics of land covers derived from original LST time series.

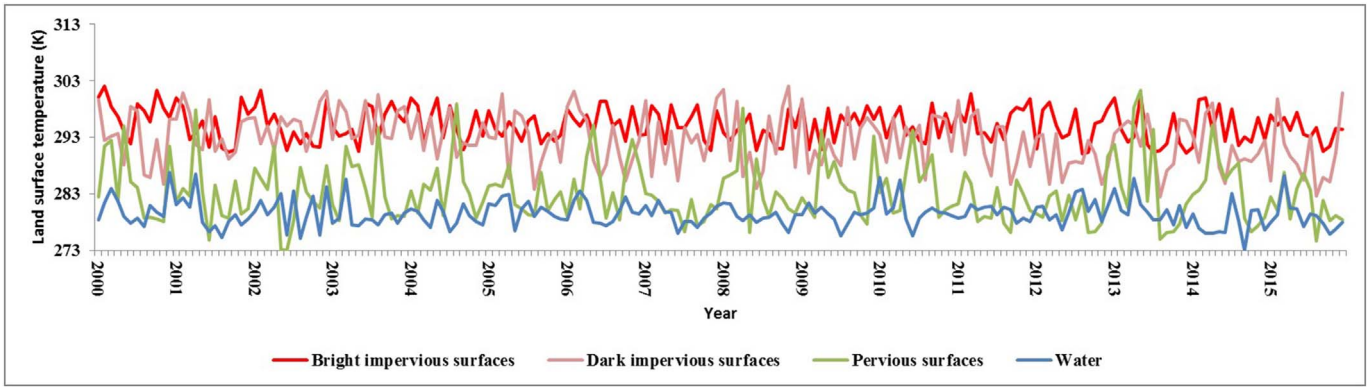

Fig. 10. Temporal characteristics of land covers derived from composited monthly LST time series.

pattern of urbanization, which contribute to the management of environmental impacts, resources, and sustainable developments. Finally, monthly data of impervious surfaces would be considerably more useful in modeling urban environmental systems and ecosystems, which previously required fine temporal resolution biophysical variables.

Impervious surface maps in December from each year from 2000 to 2015 were selected as representative annual maps for subsequent analysis. Fig. 13 shows yearly December maps of impervious surfaces from 2000 to 2015.

In Fig. 13, red color represents impervious surfaces, blue color represents water bodies, and green color represents pervious surfaces. Impervious surfaces increased from 3786.33 km^2 in 2001 to 5992.31 km^2 by the end of 2015, yielding an overall increase of 58%. The whole study period was divided into four stages: (1) 2000–2004; (2) 2005–2008; (3) 2009–2011; and (4) 2012–2015. The growth rate of impervious surfaces at each stage varied from 18.04%, 10.88%, 6.45%, to 4.41%, indicating a declining trend in urbanization pace. From 2000 to 2004, several urban clusters emerged in both sides of the delta, resulting from more than a decade of leapfrog and clustering urbanization processes. After 2005, most increments of impervious surfaces were observed to be concentrated in urban areas, suggesting there was more in-fill urban development during this period. After 2009, impervious surfaces expanded from urban areas to more rural areas. Since 2012, impervious surfaces were detected more often among the urban areas, indicating that a large urban agglomeration has been forming in the PRD. In order to better understand the changes of impervious surfaces, monthly impervious surface area was plotted along with quarterly, semi-annual, and annual growth rates (Fig. 14).

Within each year, quarterly and semi-annual growth rates of impervious surfaces also varied. With respect to semi-annual growth rates of impervious surfaces, Fig. 14 suggests that for the majority of the years, the second half of each year often had higher growth rates than the first half of the year. This was mainly because most construction was completed by the end of each year. In terms of quarterly growth rates of impervious surfaces, there were not obvious patterns of change. While the second halves of some years, such as 2000, 2002, and 2003, had higher growth rates than the first halves of those years, the first quarters often had the highest growth rates among all time periods. In conclusion, growth rates can vary with month, season, or year, and mapping impervious surfaces by month was needed for the PRD.

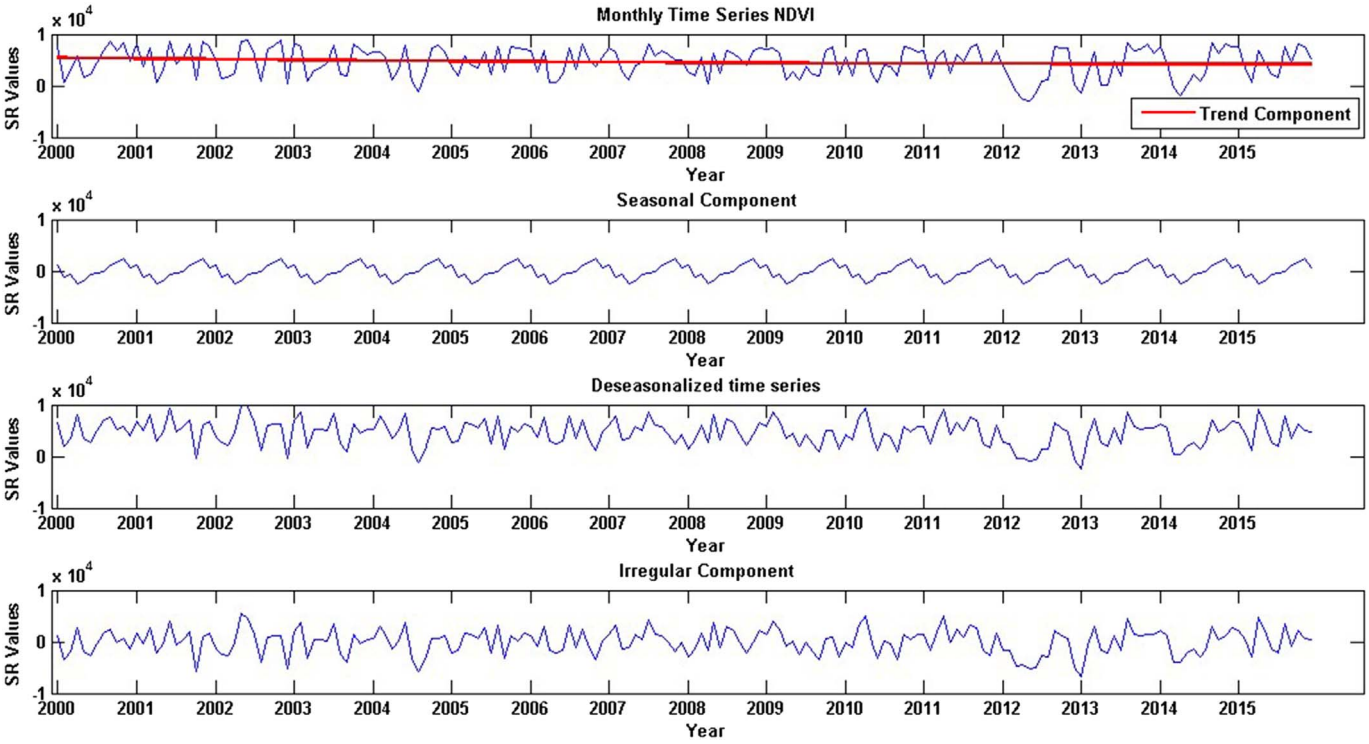

Fig. 11. Time series components of a pervious surface pixel in monthly NDVI time series.

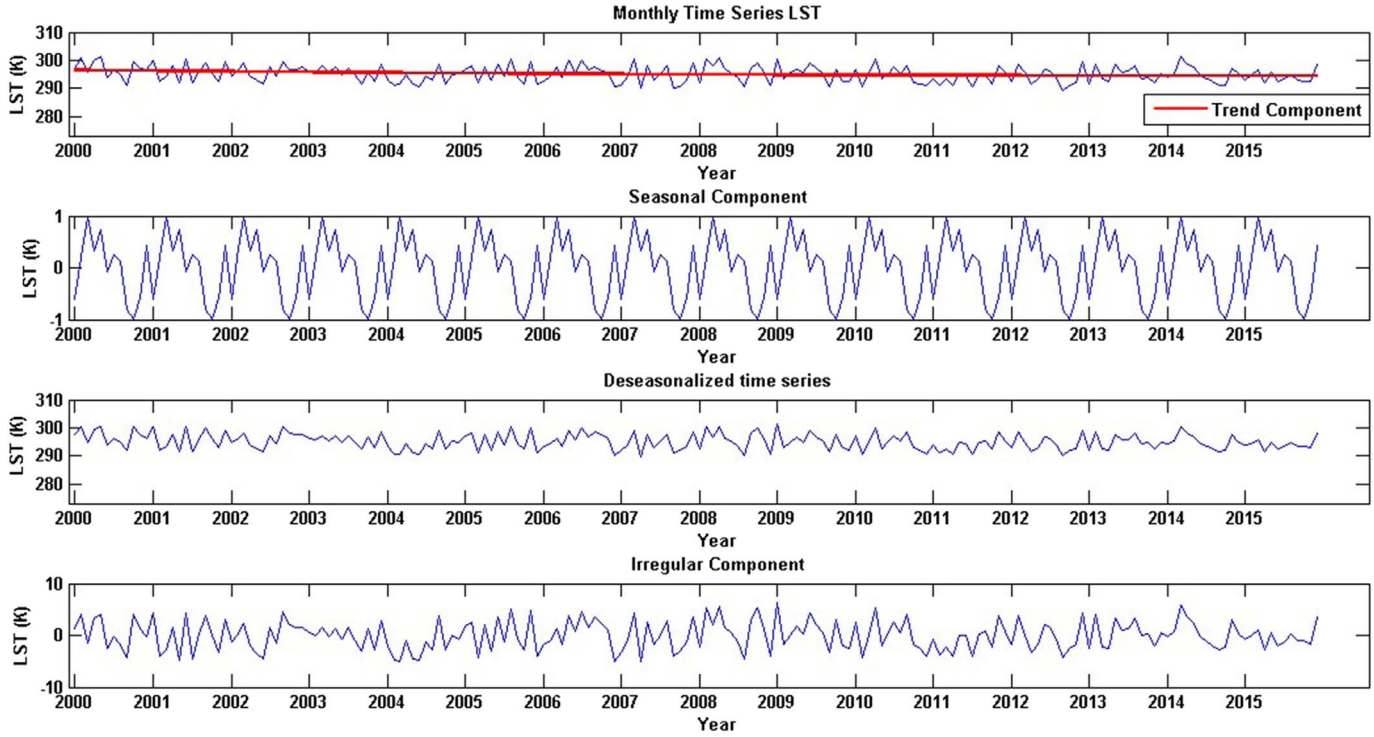

Fig. 12. Time series components of an impervious surface pixel in monthly LST time series.

Since the highest annual growth rate was observed in 2003, monthly maps in this year were displayed in Fig. 15 to analyze monthly spatial-temporal change of impervious surfaces. Impervious surfaces increased in the first quarter by 1.33%. However, in the second quarter of the year, monthly impervious surfaces did not vary greatly in size and shape, and the quarterly growth rate was only 0.22%. In the third and fourth quarters, impervious surfaces expanded from urban areas to suburban areas, and the quarterly growth rates reached 0.90% and 0.87, respectively.

4.4. Accuracy assessment

In this study, confusion matrix was computed as the quantitative method of assessing clustering accuracy since it has been successfully applied in accuracy assessment (Foody, 2002). In order to ensure time consistency, reference data were derived from stable areas. Stable areas were identified as unchanged land cover areas in stacked clear-sky BCI images. With the aid of historical Google Earth imagery, pure pixels in the stable areas were selected. The stratified random sampling scheme was applied to select 500 samples per class from each image as the reference data for accuracy assessment. Half of them were used for training, while the others were used for accuracy assessment.

Annual classification accuracies from 2000 to 2015 and monthly classification accuracies in 2015 were assessed to verify the effectiveness of the proposed method. Fig. 16 shows the accuracies regarding the annual classifications of different land covers.

The yearly overall classification accuracy yielded a rate as high as 89.36%. Classification accuracy in 2002 (85.54%) was lower than that in 2001 (85.67%), due largely to fewer images (21 in 2002 vs, 29 in 2001). Average cloud cover percentages in these two years were almost the same, with 49.79% in 2002 and 46.93% in 2001. The same situation occurred in 2009 and 2010. Average cloud cover percentages of the two years were 42.59% and 43.08%, respectively, but there were only 19 images in 2010 as compared to 32 images in 2009. In 2005, the producer's accuracy of bright impervious surfaces and user's accuracy of pervious surfaces were very low, because half of the available Landsat images in 2005 were SLC-off data and the percentage of cloud cover data without SLC-off data was as high as 39.28%. Table 1 shows the influence of temporal resolution in the proposed method. Fig. 16 further shows the effectiveness of temporal resolution, as the classification accuracy increased slightly over time. This is due to higher temporal resolution (more images) for the more recent time series data; this allows for temporal features to be extracted from the data.

Areas with the lowest accuracy were largely suburban areas, because impervious surfaces mixed with other land covers within mixed pixels. Additionally, low accuracy was detected in suburban areas where there was a discrete distribution of bright impervious surfaces, instead of being continuous. In these areas, cluster centers were difficult to identify. Cloud-contaminated areas over a long time span may also contribute to low accuracy due to the error caused by the gap filling.

Table 1
DTW distances of land covers derived from original time series, monthly time series and temporal features.

	BIS			DIS			PS			W		
	Ot	Mt	Tt	Ot	Mt	Tt	Ot	Mt	Tt	Ot	Mt	Tt
BIS	0.37	0.49	0.24	0.26	0.35	0.48	0.84	0.85	0.91	0.83	0.92	0.95
DIS	–	–	–	0.22	0.29	0.18	0.78	0.71	0.86	0.89	0.9	0.95
PS	–	–	–	–	–	–	0.25	0.1	0.47	0.77	0.94	0.94
W	–	–	–	–	–	–	–	–	–	0.42	0.25	0.12

Note: BIS-Bright Impervious Surfaces, DIS-Dark Impervious Surfaces, PS-Pervious Surfaces, W-Water; Ot-Original time series, Mt.-Monthly time series, Tt-Temporal features.

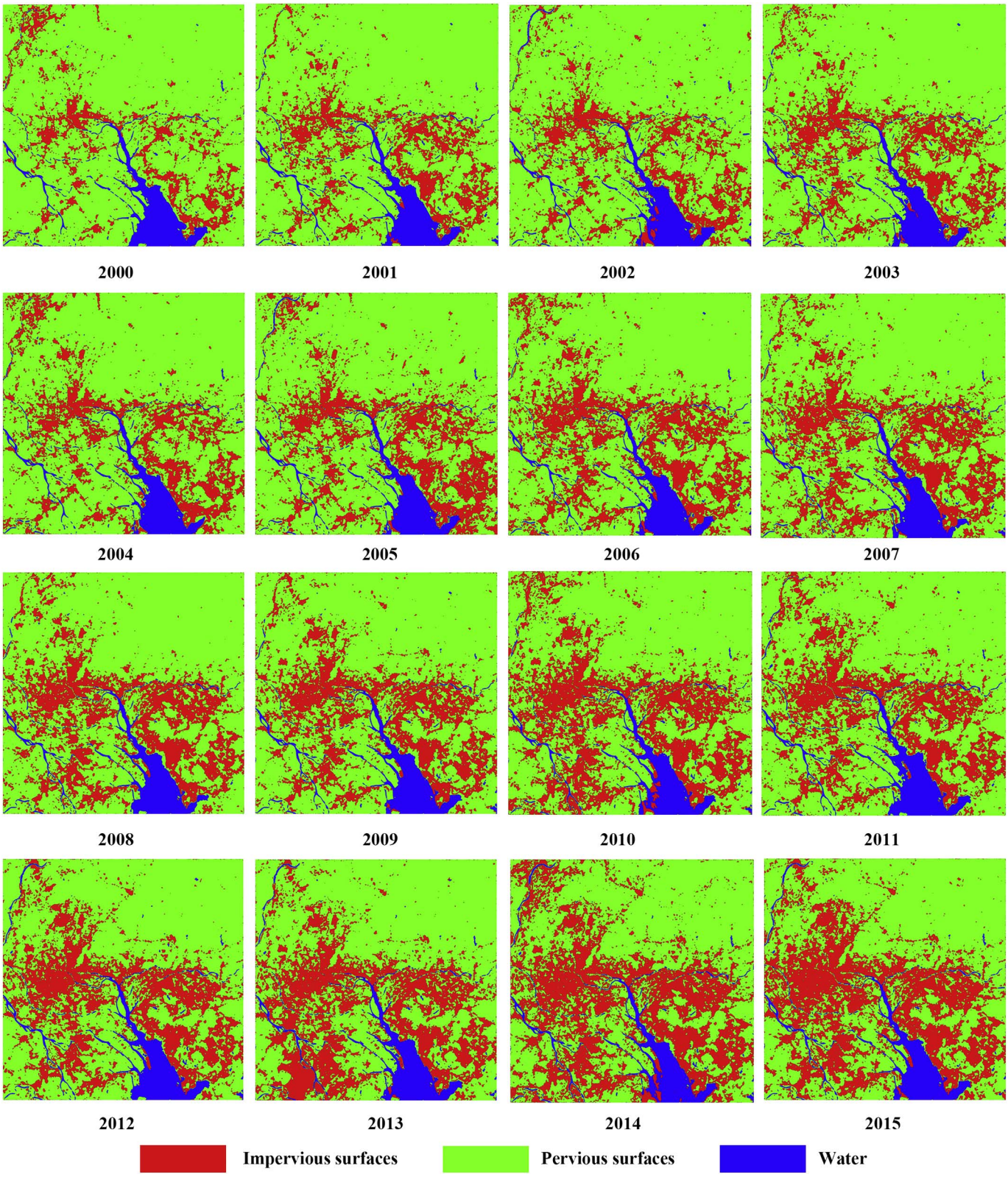

Fig. 13. Yearly December maps of impervious surfaces in the Pearl River Delta, China, 2000–2015. (For interpretation of the references to color in this figure, the reader is referred to the web version of this article.)

Although cloud cover was removed by using NSPI and SLC-off data was filled by GNSPI, the difference between estimated and observed values could lead to errors in classification.

For assessing classification accuracies in 2015, we conducted fieldwork on current land use and land cover (impervious surfaces) and urban morphology to obtain ground truth data in the PRD, China, in January 4–8, 2016. Field surveys collected information on surface cover conditions, including agriculture, water, barren land, horticulture, wetland, and impervious surfaces. The stratified random scheme was adopted to select 400 sample sites from a cloud-free Landsat OLI image

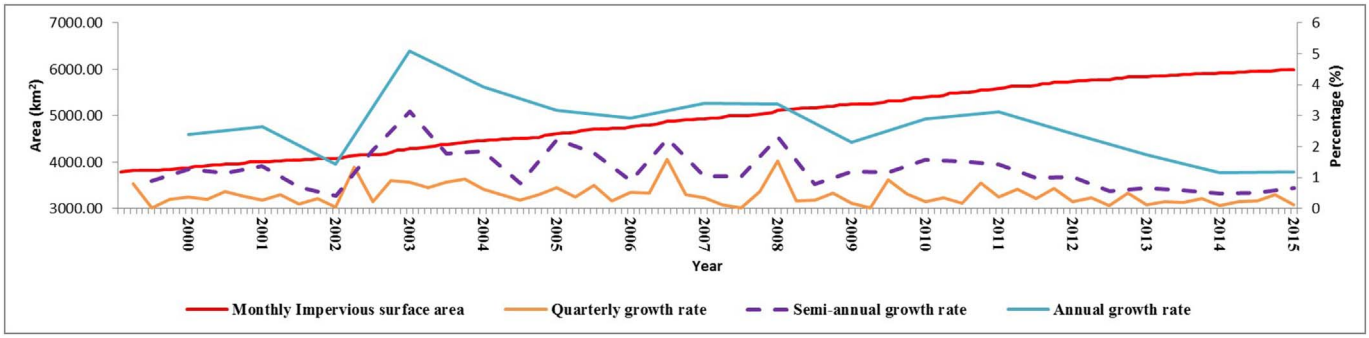

Fig. 14. Monthly dynamics of impervious surface areas, and quarterly, semi-annual, annual growth rates of impervious surfaces in the Pearl River Delta from 2000 to 2015.

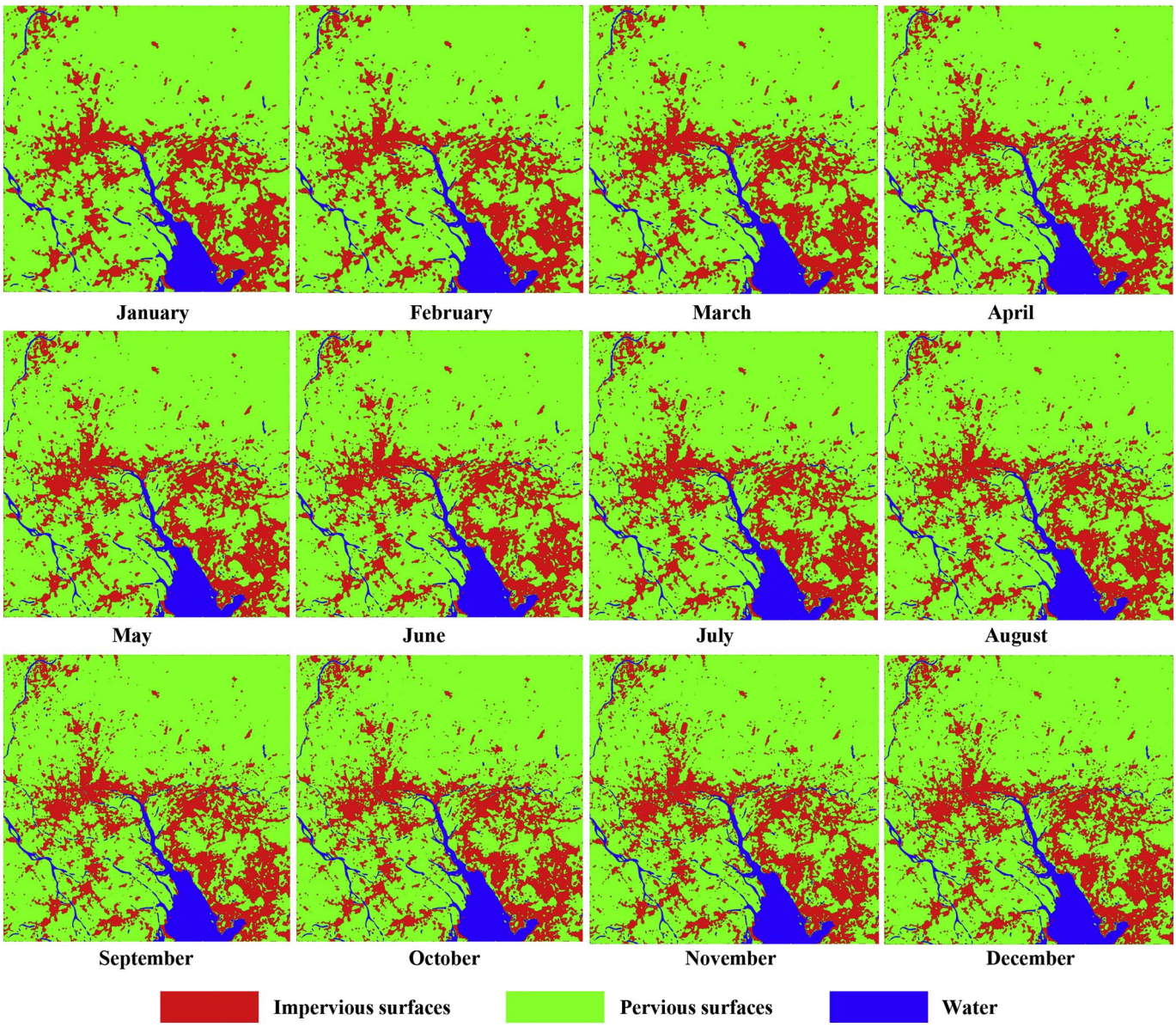

Fig. 15. Monthly maps of impervious surfaces in the Pearl River Delta in 2003.

acquired on October 18, 2015 and Google Earth images (0.3 m spatial resolution). For each sample site, hand-held global positioning system (GPS) receivers, digital cameras, and daily logs were used to record observations. Given 30 m Landsat OLI data and the requirement of ± 0.5 pixel (15 m) in locational accuracy, the minimum sample size was set to 60 m × 60 m. These sample sites were distributed in Dongguan, Guangzhou, Foshan, and Shenzhen. GPS-Photo Link was used to link digital photos and descriptions of land cover conditions in the field to the base maps. Fig. 17 shows five selected sampling sites. The background image was a natural color composite image using the Landsat OLI image bands 4, 3, and 2. Five types of land cover samples were shown in the right side of the figure. Blue polygons were

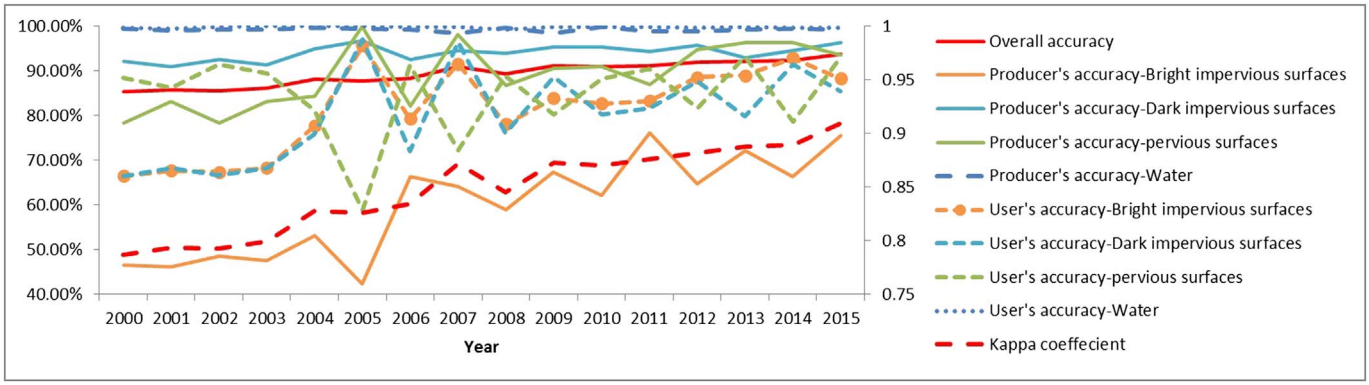

Fig. 16. Annual classification accuracies of proposed method from 2000 to 2015.

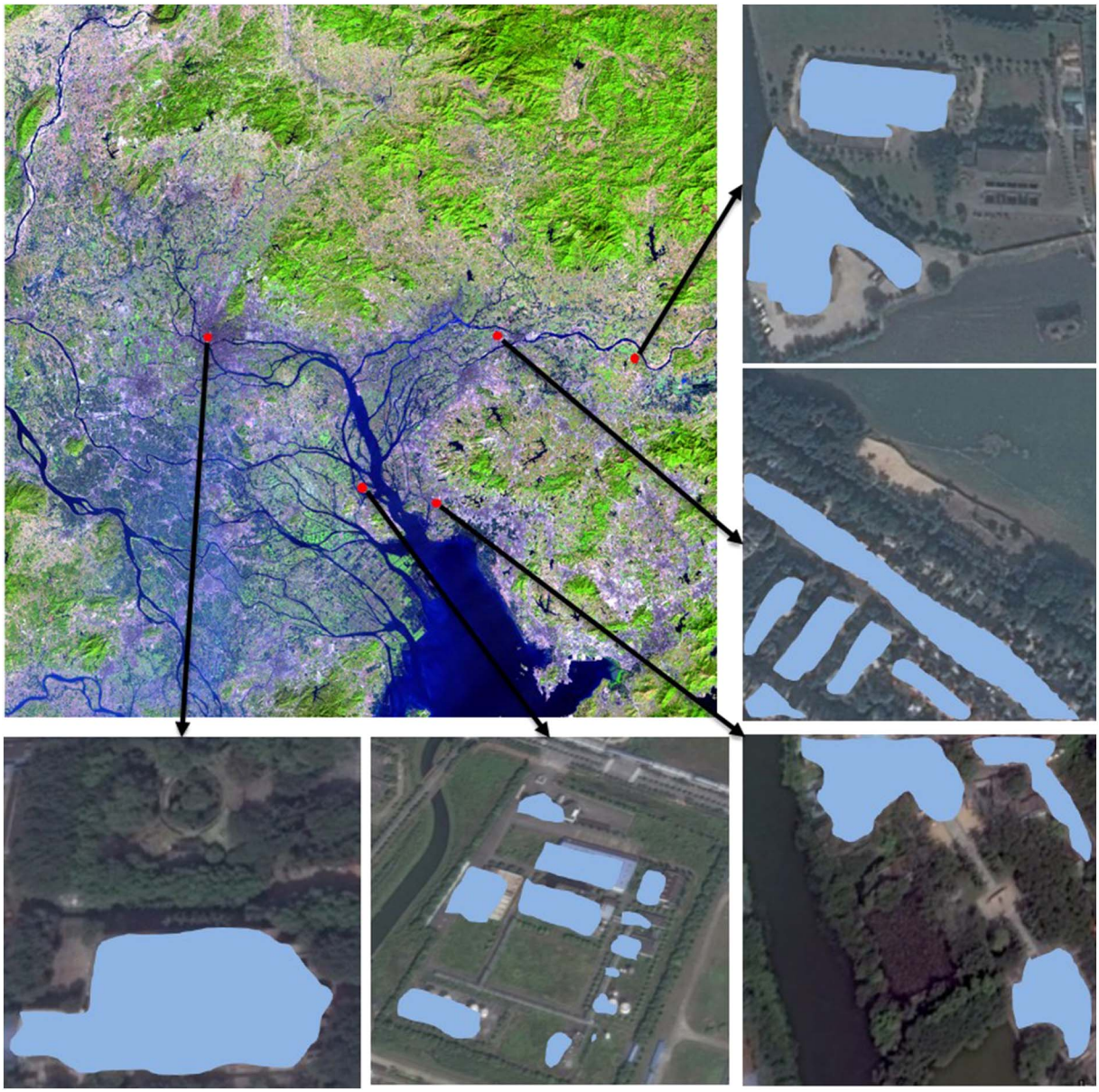

Fig. 17. Distribution of selected sample sites for impervious surfaces mapping. (For interpretation of the references to color in this figure, the reader is referred to the web version of this article.)

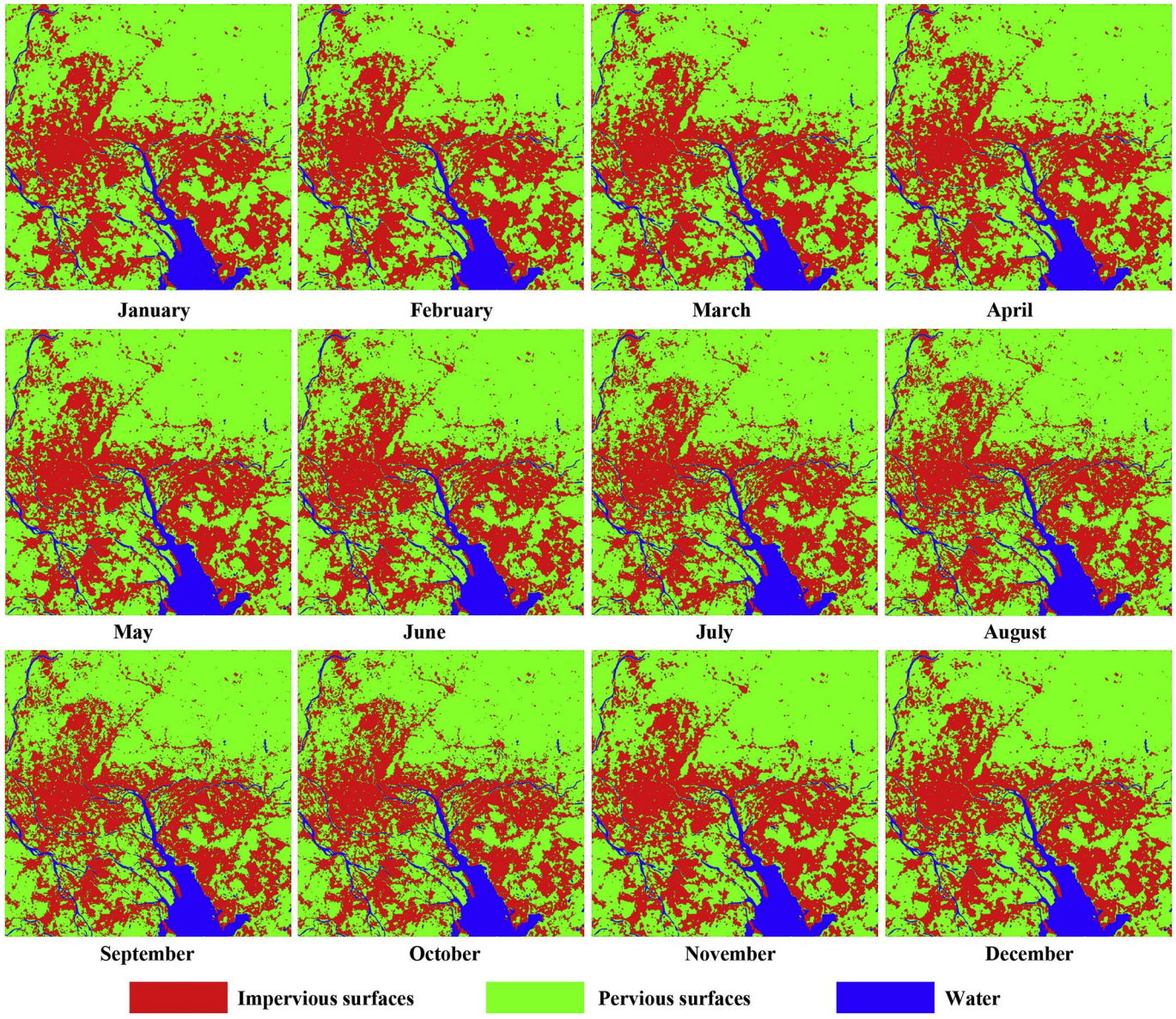

Fig. 18. Monthly maps of impervious surfaces in 2015. (For interpretation of the references to color in this figure, the reader is referred to the web version of this article.)

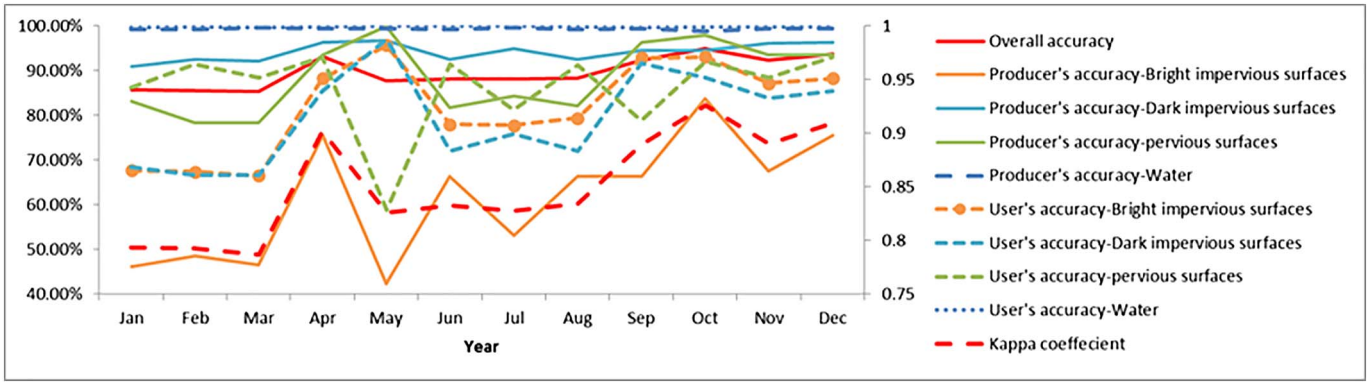

Fig. 19. Monthly classification accuracies of land covers in 2015.

impervious surfaces in each scene, including building roofs and dense human settlements.

Fig. 18 shows monthly maps of impervious surfaces in 2015, where red color represents impervious surfaces, blue color represents water bodies, and green color represents pervious surfaces. Monthly impervious surface areas did not vary significantly in size and shape. Monthly classification accuracies of land covers in 2015 were computed with the ground truth data. Fig. 19 shows that the average classification

Table 2
Selected Landsat images.

Landsat image ID	Acquired date	Cloud cover (%)
LT51220442000346BJC00	2000/12/11	41.64
LT51220442001364BJC00	2001/12/30	0.01
LT51220442002351BJC00	2002/12/17	79.36
LE71220442003362BKT00	2003/12/28	0.05
LE71220442004349EDC00	2004/12/14	1.58
LE71220442005351EDC00	2005/12/17	0.1
LT51220442006362BJC01	2006/12/28	0.01
LE71220442007341EDC01	2007/12/7	0.17
LT51220442008352BJC00	2008/12/17	0.03
LT51220442009338BJC00	2009/12/4	6.39
LE71220442010365EDC00	2010/12/31	0.06
LE71220442011352EDC00	2011/12/18	2.21
LE71220442012307EDC00	2012/11/2	0.04
LE71220442013341EDC00	2013/12/7	0.02
LE71220442014344EDC00	2014/12/10	33.98
LE71220442015363EDC00	2015/12/29	75.01

accuracy during the first three months was 85.48%. In April, classification accuracy increased to 93.01%, because this month did not encounter serious cloud contamination. The average cloud cover in April was 21.41%. From May to August, classification accuracies were around 88%, due to increased clouds during the wet season. Classification accuracy went up to over 92% after September. The highest classification accuracy was observed in October as there was one cloud free image, despite the average cloud cover was 25.37%.

In order to demonstrate the accuracy improvements of the proposed method, semi-supervised FCM and SVM (Support Vector Machine) with the same parameters and training data were used to classify the December images each year. One November image was used in 2012 because the December images were not available. The selected Landsat images were shown in Table 2.

Table 3 shows the annual classification accuracy of the proposed method, semi-supervised FCM, and SVM from 2000 to 2015. Generally, the classification accuracies of semi-supervised FCM were low. SVM performed better than semi-supervised FCM, while the proposed method yielded the best classification accuracy. The classification accuracies of the proposed method in 2000 and 2002 were similar to 2001. Additionally, in 2015, the classification accuracy reached 93.64%. In contrast, semi-supervised FCM had the lowest classification accuracy in 2000, 2002, 2014, and 2015, because the cloud cover reached 41.64%, 79.36%, 33.98%, and 75.01%, respectively. Furthermore, classification accuracies of SVM in these years were also lower than other years. It can be concluded that the proposed method largely eliminated the effect of cloud cover and improved the classification accuracy of mapping impervious surfaces.

Table 3
Annual classification accuracies of the proposed method, semi-supervised FCM and SVM.

Year	Proposed method	semi-supervised FCM	SVM
2000	85.22%	76.77%	80.84%
2001	85.67%	79.18%	84.13%
2002	85.54%	78.16%	79.08%
2003	86.01%	80.02%	81.76%
2004	88.02%	79.31%	86.56%
2005	87.68%	79.64%	84.59%
2006	88.24%	82.25%	86.31%
2007	90.88%	83.11%	87.56%
2008	89.27%	80.04%	86.20%
2009	91.15%	83.28%	89.00%
2010	90.98%	84.70%	87.50%
2011	91.16%	85.82%	90.02%
2012	91.79%	82.45%	86.93%
2013	92.16%	84.31%	90.15%
2014	92.33%	76.55%	78.49%
2015	93.64%	71.16%	75.96%

5. Discussion and conclusions

While previous methods focused mainly on impervious surface dynamics at annual or decadal scales, this study proposed a new method for mapping monthly impervious surface dynamics by using the synthetic time series of Landsat and MODIS imagery. The proposed methodology was applied to the Pearl River Delta in China from 2000 to 2015, where frequent clouds and rains exist from April to September and cloud-free Landsat imagery was limited. In order to obtain a dense Landsat data series and to improve temporal resolution, the fusion of Landsat data and MODIS data was conducted to generate synthetic Landsat images. These synthetic images were combined with original Landsat images to create a complete monthly NDVI and LST time series. Temporal features that derived from time series decomposition were used for classifying land covers. The average overall classification accuracy reached 89.36%.

The main contributions of this study are as follows: First, this study developed a method for generating a complete monthly Landsat time series by fusing available Landsat data and MODIS data, which improved the temporal resolution of Landsat observation and eliminated uncertainty in data analysis caused by unevenly Landsat time series. The appropriate time scale for impervious surface mapping was largely dependent on the actual timing of land cover change. This study showed that maps of impervious surfaces at annual or decadal scales were not sufficient to characterize and analyze the rapid urbanization in the PRD. Monthly impervious surface dynamics can not only build a strong relationship between temporal and spatial patterns of urban expansion on a fine time scale, but also they can facilitate the establishment of a relationship between urban expansion and urban environmental system, ecosystem, and social-economics. Secondly, this study extracted temporal features by using the time series decomposition technique, which was helpful for increasing the time series separability of land covers. Time series components -seasonal, trend, and irregular components - helped in identifying recurring temporal patterns and temporal trends in land cover changes. Additionally, temporal features can effectively detect any anomalies in data by using the seasonally adjusted time series.

However, there were a few issues that need to be examined further. One issue is that the fuzzy clustering algorithm should not be utilized discrete data, because the algorithm was ineffective for detecting local outliers. Detected discrete points were largely global outliers. Additionally, the clustering algorithm was sensitive to parameters and was highly dependent on the initialization of centroids. Nevertheless, it may be difficult to select effective initial centroid clusters randomly for each image in the time series. Uncertainty caused by the selection of initial centroid clusters can result in inconsistent clustering results. One method that can be used to address this issue is to build an initialization scheme that initializes centroids to be generally distant from each other. Secondly, this study used the fuzzy clustering method where each pixel may belong to more than one land cover class with different membership. Thus, the fuzzy clustering was able to model uncertainty typically involved in land cover classification, but was unable to solve the problem of mixed pixels since impervious surfaces may occupy an area smaller than 30mX30m. Future studies may utilize a hybrid technique of fuzzy clustering and spectral mixture analysis to assess the benefit of time series features for sub-pixel impervious surface mapping. The lowest producer's accuracies were observed with bright impervious surfaces, which indicates the failure of the proposed method to recognize them. The majority of the omission errors occurred in the suburban areas where there was a discrete distribution of bright impervious surfaces. Additionally, it was difficult to select cluster centers for bright impervious surfaces in the suburban areas, which also led to low producer's accuracies.

Acknowledgements

We thank anonymous reviewers and editor for their constructive comments and suggestions. Further, we acknowledge the financial support by Postdoctoral Innovative Talent Support Plan to Lei Zhang (BX201700175).

References

Bezdek, J.C., Ehrlich, R., Full, W., 1984. FCM: the fuzzy c-means clustering algorithm. Comput. Geosci. 10 (2–3), 191–203.
Cleveland, W.P., Tiao, G.C., 1976. Decomposition of seasonal time series: a model for the census X-11 program. J. Am. Stat. Assoc. 71 (355), 581–587.
Egrioglu, E., Aladag, C.H., Yolcu, U., 2013. Fuzzy time series forecasting with a novel hybrid approach combining fuzzy c-means and neural networks. Expert Syst. Appl. 40 (3), 854–857.
Esch, T., Himmler, V., Schorcht, G., Thiel, M., Wehrmann, T., Bachofer, F., ... Dech, S., 2009. Large-area assessment of impervious surface based on integrated analysis of single-date Landsat-7 images and geospatial vector data. Remote Sens. Environ. 113 (8), 1678–1690.
Foody, G.M., 2002. Status of land cover classification accuracy assessment. Remote Sens. Environ. 80 (1), 185–201.
Fu, T.C., 2011. A review on time series data mining. Eng. Appl. Artif. Intell. 24 (1), 164–181.
Futschik, M.E., Kasabov, N.K., 2002. Fuzzy clustering of gene expression data. In: Fuzzy Systems, 2002. FUZZ-IEEE'02. Proceedings of the 2002 IEEE International Conference on. Vol. 1. IEEE, pp. 414–419.
Gao, F., Masek, J., Schwaller, M., Hall, F., 2006. On the blending of the Landsat and MODIS surface reflectance: predicting daily Landsat surface reflectance. IEEE Trans. Geosci. Remote Sens. 44 (8), 2207–2218.
Gao, F., de Colstoun, E.B., Ma, R., Weng, Q., Masek, J.G., Chen, J., ... Song, C., 2012. Mapping impervious surface expansion using medium-resolution satellite image time series: a case study in the Yangtze River Delta, China. Int. J. Remote Sens. 33 (24), 7609–7628.
Han, Y., Wang, Y., Zhao, Y., 2010. Estimating soil moisture conditions of the greater Changbai Mountains by land surface temperature and NDVI. IEEE Trans. Geosci. Remote Sens. 48 (6), 2509–2515.
Hilker, T., Wulder, M.A., Coops, N.C., Linke, J., McDermid, G., Masek, J.G., ... White, J.C., 2009. A new data fusion model for high spatial-and temporal-resolution mapping of forest disturbance based on Landsat and MODIS. Remote Sens. Environ. 113 (8), 1613–1627.
Hu, X., Weng, Q., 2009. Estimating impervious surfaces from medium spatial resolution imagery using the self-organizing map and multi-layer perceptron neural networks. Remote Sens. Environ. 113 (10), 2089–2102.
Jeong, Y.S., Jeong, M.K., Omitaomu, O.A., 2011. Weighted dynamic time warping for time series classification. Pattern Recogn. 44 (9), 2231–2240.
Julien, Y., Sobrino, J.A., Mattar, C., Ruescas, A.B., Jimenez-Munoz, J.C., Soria, G., ... Cuenca, J., 2011. Temporal analysis of normalized difference vegetation index (NDVI) and land surface temperature (LST) parameters to detect change in the Iberian land cover between 1981 and 2001. Int. J. Remote Sens. 32 (7), 2057–2068.
Keogh, E., Chakrabarti, K., Pazzani, M., Mehrotra, S., 2001. Dimensionality reduction for fast similarity search in large time series databases. Knowl. Inf. Syst. 3 (3), 263–286.
Kondrashov, D., Ghil, M., 2006. Spatio-temporal filling of missing points in geophysical data sets. Nonlinear Process. Geophys. 13 (2), 151–159.
Li, S.T., Cheng, Y.C., Lin, S.Y., 2008. A FCM-based deterministic forecasting model for fuzzy time series. Comp. Math. Appl. 56 (12), 3052–3063.
Li, J., Song, C., Cao, L., Zhu, F., Meng, X., Wu, J., 2011. Impacts of landscape structure on surface urban heat islands: a case study of shanghai, China. Remote Sens. Environ. 115 (12), 3249–3263.
Liao, T.W., 2005. Clustering of time series data-a survey. Pattern Recogn. 38 (11), 1857–1874.
Lu, D., Weng, Q., 2009. Extraction of urban impervious surfaces from an IKONOS image. Int. J. Remote Sens. 30 (5), 1297–1311.
Lu, D., Moran, E., Hetrick, S., 2011. Detection of impervious surface change with multitemporal Landsat images in an urban–rural frontier. ISPRS J. Photogramm. Remote Sens. 66 (3), 298–306.
Lunetta, R.S., Johnson, D.M., Lyon, J.G., Crotwell, J., 2004. Impacts of imagery temporal frequency on land-cover change detection monitoring. Remote Sens. Environ. 89 (4), 444–454.
Lunetta, R.S., Knight, J.F., Ediriwickrema, J., Lyon, J.G., Worthy, L.D., 2006. Land-cover change detection using multi-temporal MODIS NDVI data. Remote Sens. Environ. 105 (2), 142–154.
Ma, X., Huete, A., Yu, Q., Coupe, N.R., Davies, K., Broich, M., ... Boulain, N., 2013. Spatial patterns and temporal dynamics in savanna vegetation phenology across the North Australian Tropical Transect. Remote Sens. Environ. 139, 97–115.
Mohapatra, R.P., Wu, C., 2010. High resolution impervious surface estimation. Photogramm. Eng. Remote. Sens. 76 (12), 1329–1341.
Petitjean, F., Ketterlin, A., Gançarski, P., 2011. A global averaging method for dynamic time warping, with applications to clustering. Pattern Recogn. 44 (3), 678–693.
Powell, S.L., Cohen, W.B., Yang, Z., Pierce, J.D., Alberti, M., 2008. Quantification of impervious surface in the Snohomish water resources inventory area of western Washington from 1972–2006. Remote Sens. Environ. 112 (4), 1895–1908.
Ratana, P., Huete, A.R., Ferreira, L., 2005. Analysis of Cerrado physiognomies and conversion in the MODIS seasonal-temporal domain. Earth Interact. 9 (3), 1–22.
Sexton, J.O., Song, X.P., Huang, C., Channan, S., Baker, M.E., Townshend, J.R., 2013. Urban growth of the Washington, DC–Baltimore, MD metropolitan region from 1984 to 2010 by annual, Landsat-based estimates of impervious cover. Remote Sens. Environ. 129, 42–53.
Shao, Z., Liu, C., 2014. The integrated use of DMSP-OLS nighttime light and MODIS data for monitoring large-scale impervious surface dynamics: a case study in the Yangtze River Delta. Remote Sens. 6 (10), 9359–9378.
Son, N.T., Chen, C.F., Chen, C.R., Chang, L.Y., Minh, V.Q., 2012. Monitoring agricultural drought in the Lower Mekong Basin using MODIS NDVI and land surface temperature data. Int. J. Appl. Earth Obs. Geoinf. 18, 417–427.
Vuolo, F., Mattiuzzi, M., Klisch, A., Atzberger, C., 2012. Data service platform for MODIS vegetation indices time series processing at BOKU Vienna: current status and future perspectives. In: SPIE Remote Sensing. International Society for Optics and Photonics, pp. 85380A October.
Wang, G., Garcia, D., Liu, Y., De Jeu, R., Dolman, A.J., 2012. A three-dimensional gap filling method for large geophysical datasets: application to global satellite soil moisture observations. Environ. Model Softw. 30, 139–142.
Weng, Q., 2012. Remote sensing of impervious surfaces in the urban areas: requirements, methods, and trends. Remote Sens. Environ. 117, 34–49.
Weng, Q., Fu, P., Gao, F., 2014. Generating daily land surface temperature at Landsat resolution by fusing Landsat and MODIS data. Remote Sens. Environ. 145, 55–67.
Weng, Q., Hu, X., Lu, D., 2008. Extracting impervious surfaces from medium spatial resolution multispectral and hyperspectral imagery: a comparison. Int. J. Remote Sens. 29 (11), 3209–3232.
Wu, C., Murray, A.T., 2003. Estimating impervious surface distribution by spectral mixture analysis. Remote Sens. Environ. 84 (4), 493–505.
Yang, L., Huang, C., Homer, C.G., Wylie, B.K., Coan, M.J., 2003. An approach for mapping large-area impervious surfaces: synergistic use of Landsat-7 ETM + and high spatial resolution imagery. Can. J. Remote. Sens. 29 (2), 230–240.
Yuan, F., Bauer, M.E., 2007. Comparison of impervious surface area and normalized difference vegetation index as indicators of surface urban heat island effects in Landsat imagery. Remote Sens. Environ. 106 (3), 375–386.
Yuan, F., Wu, C., Bauer, M.E., 2008. Comparison of spectral analysis techniques for impervious surface estimation using Landsat imagery. Photogramm. Eng. Remote. Sens. 74 (8), 1045–1055.
Zhang, L., Weng, Q., 2016. Annual dynamics of impervious surface in the Pearl River Delta, China, from 1988 to 2013, using time series Landsat imagery. ISPRS J. Photogramm. Remote Sens. 113, 86–96.
Zhang, Y., Odeh, I.O., Han, C., 2009. Bi-temporal characterization of land surface temperature in relation to impervious surface area, NDVI and NDBI, using a sub-pixel image analysis. Int. J. Appl. Earth Obs. Geoinf. 11 (4), 256–264.
Zhang, Y., Zhang, H., Lin, H., 2014. Improving the impervious surface estimation with combined use of optical and SAR remote sensing images. Remote Sens. Environ. 141, 155–167.
Zhu, Z., Woodcock, C.E., 2012. Object-based cloud and cloud shadow detection in Landsat imagery. Remote Sens. Environ. 118, 83–94.
Zhu, X., Chen, J., Gao, F., Chen, X., Masek, J.G., 2010. An enhanced spatial and temporal adaptive reflectance fusion model for complex heterogeneous regions. Remote Sens. Environ. 114 (11), 2610–2623.
Zhu, X., Gao, F., Liu, D., Chen, J., 2012a. A modified neighborhood similar pixel interpolator approach for removing thick clouds in Landsat images. IEEE Geosci. Remote Sens. Lett. 9 (3), 521–525.
Zhu, X., Liu, D., Chen, J., 2012b. A new geostatistical approach for filling gaps in Landsat ETM + SLC-off images. Remote Sens. Environ. 124, 49–60.
Zhu, X., Helmer, E.H., Gao, F., Liu, D., Chen, J., Lefsky, M.A., 2016. A flexible spatiotemporal method for fusing satellite images with different resolutions. Remote Sens. Environ. 172, 165–177.